Neuron, Vol. 45, 105–117, January 6, 2005, Copyright ©2005 by Elsevier Inc. DOI 10.1016/j.neuron.2004.12.016

Perisomatic Feedback Inhibition Underlies Cholinergically Induced Fast Network Oscillations in the Rat Hippocampus In Vitro

Edward O. Mann,[1,*] Jillian M. Suckling,[1,2] Norbert Hajos,[1,3] Susan A. Greenfield,[2] and Ole Paulsen[1]

[1]University Laboratory of Physiology
Oxford University
Parks Road
Oxford OX1 3PT
United Kingdom

[2]Department of Pharmacology
Oxford University
Mansfield Road
Oxford OX1 3QT
United Kingdom

[3]Institute of Experimental Medicine
Hungarian Academy of Sciences
P.O. Box 67
Budapest H-1450
Hungary

Summary

Gamma frequency network oscillations are assumed to be important in cognitive processes, including hippocampal memory operations, but the precise functions of these oscillations remain unknown. Here, we examine the cellular and network mechanisms underlying carbachol-induced fast network oscillations in the hippocampus in vitro, which closely resemble hippocampal gamma oscillations in the behaving rat. Using a combination of planar multielectrode array recordings, imaging with voltage-sensitive dyes, and recordings from single hippocampal neurons within the CA3 gamma generator, active current sinks and sources were localized to the stratum pyramidale. These proximal currents were driven by phase-locked rhythmic inhibitory inputs to pyramidal cells from identified perisomatic-targeting interneurons. AMPA receptor-mediated recurrent excitation was necessary for the synchronization of interneuronal discharge, which strongly supports a synaptic feedback model for the generation of hippocampal gamma oscillations.

Introduction

Network oscillations in the gamma frequency range (~30–100 Hz), which are a characteristic feature of the awake brain during attention, have been proposed to provide a temporal structure for various cognitive processes, including sensory binding (Singer, 1993), selective attention (Fries et al., 2001), and consciousness (Llinas et al., 1998). In the hippocampus, gamma activity has been implicated in memory processing (Jensen and Lisman, 1996; Lisman and Idiart, 1995) and is commonly observed superposed on theta-frequency oscillations (4–12 Hz) (Bragin et al., 1995; Lisman and Idiart, 1995; Hasselmo et al., 1996; Buzsaki et al., 2003; Csicsvari et al., 2003). To establish more precisely what functional role gamma oscillations may subserve, it will be necessary to elucidate the underlying mechanisms. Given the extensive knowledge of hippocampal connectivity, physiology, and neurochemical anatomy, hippocampal gamma oscillations offer an attractive opportunity to investigate the cellular processes involved.

Two largely independent gamma generators have been identified in the hippocampal formation in vivo: the dentate gyrus and the CA3-CA1 system (Bragin et al., 1995; Csicsvari et al., 2003). The gamma oscillations in the dentate gyrus are driven by extrahippocampal cortical inputs and are virtually abolished by lesions of the entorhinal cortex (Bragin et al., 1995). In contrast, the CA3-CA1 system appears to form an intrinsic intrahippocampal gamma generator, in which the oscillation is generated in the recurrent CA3 network and then propagates to CA1 (Csicsvari et al., 2003). Intrahippocampal gamma activity is associated with alternating pairs of current sinks and sources in the pyramidal cell layer and the stratum radiatum (Bragin et al., 1995; Csicsvari et al., 2003), but the precise cellular and synaptic events that generate these extracellular currents have not been determined. While it has been demonstrated that both pyramidal cells and interneurons fire phase locked to the gamma oscillation (Bragin et al., 1995; Penttonen et al., 1998; Csicsvari et al., 2003) and that CA1 pyramidal cells receive gamma frequency rhythmic inhibition (Penttonen et al., 1998), the relative contributions of recurrent excitation and somatodendritic inhibition to the extracellular sink/source distribution have not been established. Furthermore, it is not yet clear whether gamma frequency synchronization in the CA3 network arises via entrainment by an interneuronal network (Whittington et al., 1995) or from synaptic recurrent feedback loops (Freeman, 1968). Therefore, what cellular currents are being recorded as gamma oscillations in the field potential and how this activity is synchronized remain uncertain. Understanding such "current" and "rhythm" generation is necessary to determine the network state during gamma oscillations and, thus, the computational roles that this rhythm could fulfill (Buzsaki, 2002).

Network oscillations in the gamma frequency range can be induced in the hippocampus in vitro by muscarinic acetylcholine receptor (mAChR) activation (Fisahn et al., 1998; Fellous and Sejnowski, 2000). At room temperature, these oscillations can be in the beta frequency range as defined in vivo (~15–30 Hz), but fall clearly in the gamma frequency band when recorded at or above 32°C (C. Ecker et al., 2001, Soc. Neurosci., abstract; Dickinson et al., 2003). They will subsequently be referred to as fast network oscillations. Such cholinergically induced fast network oscillations share many of the features of intrahippocampal gamma oscillations in vivo, including pyramidal neurons firing at low frequencies (<5 Hz) phase locked to the oscillation and the oscillation being generated in CA3 and propagating to CA1 (Fisahn et al., 1998; Csicsvari et al., 2003). Such a model has some inherent appeal, since the hippocampus re-

*Correspondence: ed.mann@physiol.ox.ac.uk

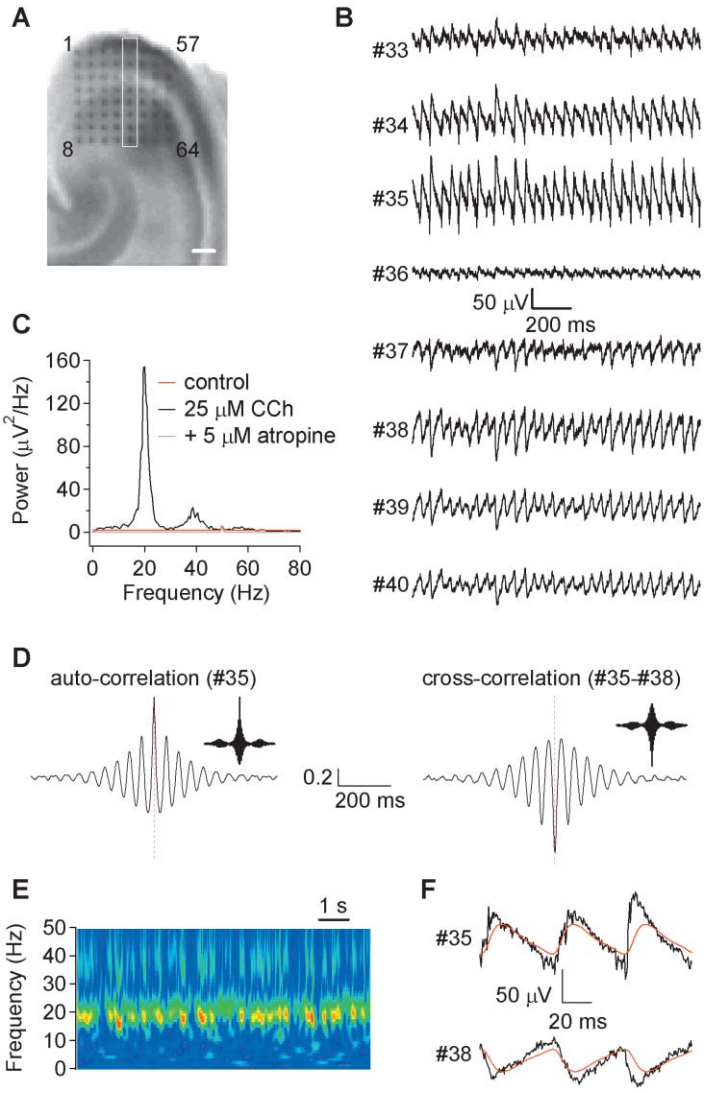

Figure 1. Carbachol-Induced Fast Network Oscillations Recorded on Multielectrode Arrays

(A) Slice mounted on 64 electrode array recording from CA3. The white box marks the column of electrodes used for presentation in (B). Electrode numbers are provided for references in the remaining panels of the figure. Scale bar, 200 μm. (B) Application of 25 μM carbachol induced oscillations in the field potentials across the different layers of CA3, with reversal of the polarity of the field oscillation in stratum lucidum (#36). (C) The power spectral density of the field oscillation in the stratum pyramidale (#35) revealed a peak at 20 Hz, with a harmonic at 40 Hz. There was no rhythmic activity prior to carbachol application (control), and the network oscillation was completely blocked by 5 μM atropine. (D) The autocorrelogram of the oscillation recorded in the stratum pyramidale (left) demonstrates robust rhythmicity in the fast network oscillation, with a period of 50 ms. The cross-correlogram between the oscillation recorded in the stratum pyramidale and distal stratum radiatum (right) reveals that these signals were π radians (180°) out of phase. Both the autocorrelogram and the cross-correlogram display side bands at ~0.86 s (inset), showing that the fast network oscillations were amplitude modulated at low frequencies (1–2 Hz). (E) The stability of the fast network oscillation over time, analyzed using wavelet transform [normalized Morlet wavelet; $\omega_0 = 6$; scales chosen to reflect unit frequencies (f) between 1 and 50 Hz; scale = $(\omega_0 + \sqrt{(2 + \omega_0^2)})/4\pi f$]. The magnitude of the wavelet transform was plotted as a function of time and frequency (corresponding to scale), with warmer colors representing increasing magnitude.

(F) Peak-to-peak cycle averages for the fast network oscillation (red traces) with an average period of 48 ms. These peak-to-peak averages fitted the time course of the underlying oscillation (black traces).

ceives a dense cholinergic projection from the medial septum/diagonal band of Broca, which plays a permissive role in the generation of hippocampal network activity (Leung, 1985; but see Lee et al., 1994). To elucidate the cellular and synaptic mechanisms underlying gamma frequency "current" and "rhythm" generation within the hippocampus, we analyzed fast network oscillations in vitro, using a combination of field recordings with planar multielectrode arrays, imaging with voltage-sensitive dyes (VSD), and recordings from individual pyramidal cells and interneurons. Our data demonstrate that cholinergically induced fast network oscillations are mediated by rhythmic perisomatic inhibition, which is synchronized by recurrent synaptic excitation.

Results

Muscarinic Receptor Activation Induces Fast Network Oscillations in the CA3 Region of the Hippocampus

To monitor field potentials, hippocampal slices were mounted on 8 × 8 planar multielectrode arrays with 100 μm spacing (Oka et al., 1999; Shimono et al., 2000) oriented across the different layers of hippocampal CA3 (see Figure 1A). Application of 25 μM carbachol induced persistent oscillations that could be recorded in all layers of the CA3 (Figure 1B), with a mean frequency of 18.9 ± 0.5 Hz at room temperature and a mean peak power of 55 ± 18 μV^2/Hz (n = 25; see Figure 1C), and often could be amplitude modulated at low frequencies (1–2 Hz; 11 of 25 slices; Figure 1D). The carbachol-induced fast network oscillations were completely blocked by the selective mAChR antagonist atropine (n = 12; Figure 1C).

The phase of the carbachol-induced oscillations reversed steeply across the stratum lucidum of the CA3 subfield (Figure 1B), with oscillations in the stratum pyramidale and distal stratum radiatum being π radians (180 degrees) out of phase (Figure 1D). Such phase reversal is expected, as changes in the extracellular field potential predominantly reflect the flow of currents in circuits along the somatodendritic axis of pyramidal cells. To analyze the mechanisms underlying these currents, peak-to-peak cycle averages were calculated for the

fast network oscillations (see Experimental Procedures). Such calculation of cycle averages assumes that the oscillation is stable and persistent. Consequently, the time-frequency characteristics of fast network oscillations were analyzed using wavelet analysis (Morlet wavelet, $\omega_0 = 6$), which does not assume stationarity and is sensitive to discontinuities (Torrence and Compo, 1998). The wavelet magnitude spectrum revealed that the oscillation frequency was stable over time and that the oscillation amplitude often showed low-frequency modulation (Figure 1E), consistent with the results from the Fourier power spectrum and autocorrelation analysis (see Figures 1C and 1D). Peak-to-peak averaging was therefore justified, and the resulting cycle averages fitted closely to the recorded responses (mean period, 48.2 ± 1.3 ms; Figure 1F).

Distribution of Current Sinks and Sources in the CA3 Region during Fast Network Oscillations

To accurately localize the sinks and sources of extracellular currents within the CA3, current-source density (CSD) profiles were constructed from cycle averages (Mitzdorf, 1985). CSD analysis of gamma oscillations in the hippocampus in vivo has been performed mainly in one dimension (1D) across the strata, assuming that extracellular currents orthogonal to the recording probe have a minimal effect on the spatial sink/source profile (see Holsheimer, 1987). This might not necessarily be justified in the centripetally organized CA3, so we started by comparing 1D and 2D CSD profiles. Both CSD methods revealed alternating sink and source pairs in the stratum pyramidale and distal stratum radiatum (Figure 2). There were small quantitative differences in the CSD analysis between the two methods (Supplemental Figure S1 [http://www.neuron.org/cgi/content/full/45/1/105/DC1/]), but as CSD analysis was subsequently used only for qualitative comparisons, 1D and 2D CSD were considered interchangeable.

Perisomatic Currents Are the Active Events Driving Sink-Source Pairs in the CA3 Region during Fast Network Oscillations

Analysis of the CSD profiles of network oscillations reveals the sinks and sources of extracellular currents, but does not distinguish between the active current generators and passive return currents. For example, a sink in the stratum pyramidale and its corresponding source in the stratum radiatum could reflect somatic excitation and/or dendritic inhibition. To elucidate the active events, CSD analysis was combined with imaging using a neuronally selective voltage-sensitive dye, Di-4-ANEPPS (Tominaga et al., 2000), to reveal the voltage changes accompanying the extracellular currents. It was found that current sinks in the stratum pyramidale with corresponding sources in the distal stratum radiatum were followed by depolarization in the perisomatic regions of CA3 pyramidal neurons, which then propagated into the apical dendrites (Figure 3A). The opposite sink/source pair preceded a hyperpolarization at perisomatic sites, with a subsequent hyperpolarization in the apical dendrites (Figure 3A). This pattern was consistent over all 25 slices tested (Figure 3B), with changes in fractional fluorescence during fast network activity, representing

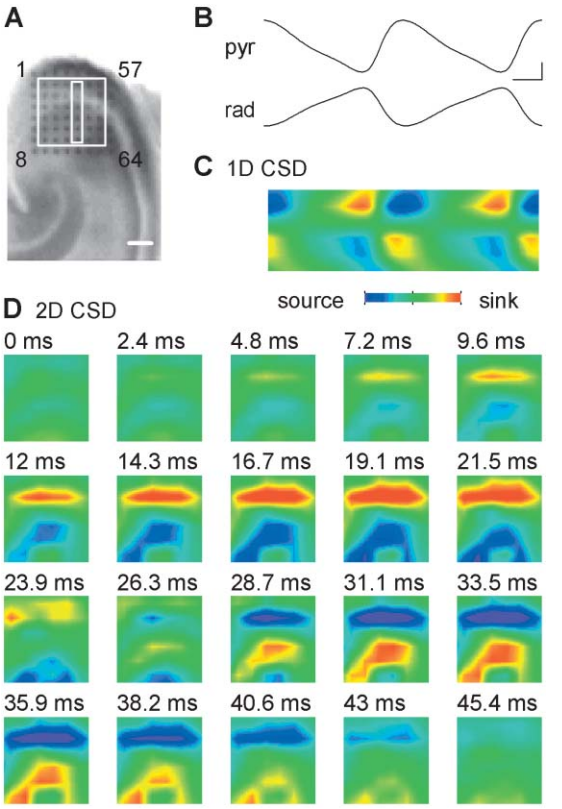

Figure 2. Spatial Pattern of Current Sinks and Sources during Fast Network Oscillations

(A) Multielectrode arrays were used to calculate 1D and 2D CSD profiles across CA3 for carbachol-induced fast network oscillations. The white rectangle marks the column of six electrodes used for 1D CSD profiles. The large white box marks the area of 36 electrodes included in the 2D CSD profiles. Electrode numbers are provided for reference. Scale bar, 200 μm.

(B) Examples of peak-to-peak cycle averages from the stratum pyramidale (#35) and distal stratum radiatum (#38), which were used to construct CSD profiles. Scale bars, 20 μV and 10 ms.

(C) Linearly interpolated 1D CSD profile from the column of electrodes shown in (A), temporally aligned with peak-to-peak cycle averages in (B). The 1D CSD profile displays alternating current sink (red) and source (blue) pairs in the stratum pyramidale and stratum radiatum.

(D) 2D CSD profile for all 36 electrodes marked in (A), sampled every ~2.4 ms. The alternating current sink/source pairs in the stratum pyramidale and stratum radiatum were evident across the extent of CA3. Color coding for sinks (red) and sources (blue) on same scale as for (C).

membrane voltage changes that varied significantly across the CA3b somatodendritic axis [RM ANOVA, $F_{(1.9, 46.1)} = 13.2$, $p < 0.001$]. These changes were most prominent in the stratum pyramidale (pyramidale versus distal radiatum; $\Delta F/F = 6.2 \pm 1.0$ versus $3.8 \pm 0.6 \times 10^{-5}$; $p < 0.001$; see Figure 3Bi). The maximum rate of increase in fractional fluorescence in the stratum pyramidale preceded that in the stratum radiatum by 0.5 ± 0.1 radians (28.6 ± 6.6 degrees; 4.0 ± 0.9 ms) (statistical analysis performed on delays relative to peak field potential in distal radiatum; $p < 0.001$; see Figure 3Bii). The maximum negative change in the optical signal occurred in the stratum pyramidale (0.6 ± 0.1 radians,

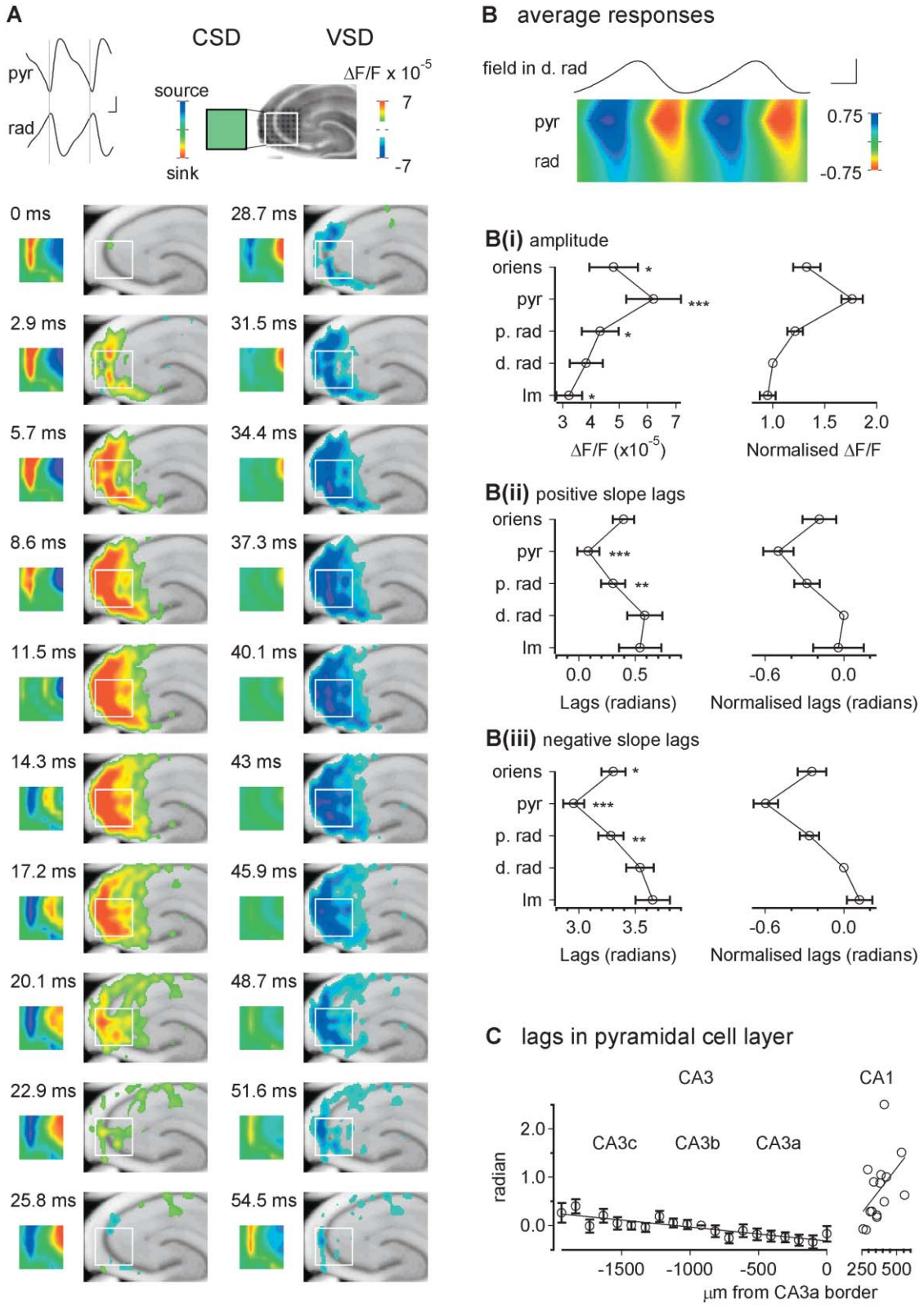

Figure 3. Voltage-Sensitive Dye Imaging of the Active Current Sinks and Sources Underlying Fast Network Oscillations

(A) VSD imaging using 200 μM Di-4-ANEPPS. Carbachol-induced oscillations were simultaneously recorded with multielectrode arrays. Examples of peak-to-peak cycle averages from the stratum pyramidale (pyr) and stratum radiatum (rad) are shown. For presentation, the 2D CSD profile from the inner 36 electrodes was displaced to the left, and pseudocolor images of the VSD signal were superposed on the image of the slice. The panel shows the 2D CSD profile sampled every ~2.9 ms. In the stratum pyramidale, current sinks (red) were followed by a

34.0 ± 5.3 degrees; 4.8 ± 0.8 ms) prior to that in the distal stratum radiatum ($p < 0.001$; see Figure 3Biii). Thus, the current sinks and sources in the stratum pyramidale appeared to represent the active events driving fast network oscillations, producing predominantly passive return currents in the stratum radiatum.

The changes in membrane voltage during fast network oscillations, revealed by imaging with voltage-sensitive dyes, were almost synchronous across the CA3 pyramidal cell layer (Figure 3A). Quantitatively, however, there were small, but significant, phase differences between the different CA3 subsegments. The time of the maximum negative slope in the optical signal was sampled for 20 equidistant points along the pyramidal cell layer of CA3 in each slice. This phase varied significantly across the CA3 stratum pyramidale [RM ANOVA, $F_{(8.3, 132.4)} = 4.34$, $p < 0.001$], showing a significant linear increase from CA3a to CA3c [RM ANOVA, $F_{(1, 16)} = 13.3$, $p < 0.01$] (Figure 3C). The average delay between the most extreme points in CA3a and CA3c was 0.6 radians (31.9 degrees; 4.5 ms) over a distance of approximately 2 mm. This result represents an average feature of the oscillation and does not suggest that the oscillation is exclusively generated in CA3a, as in some slices, rather than lagging, the CA3b/CA3c led the CA3a. Moreover, when the CA3a and CA3c were isolated by a physical cut, both subareas independently generated fast network oscillations (data not shown). The limited dimensions of the multielectrode probes precluded a detailed analysis of the fast network oscillations using field potentials. Nevertheless, in slices in which oscillations in the pyramidal cell layer could be recorded in the CA3a/CA3c relative to a central point in CA3b, there was a trend for the oscillations to be delayed in CA3c relative to CA3a (±200–600 μm from CA3b), consistent with the VSD data, but this delay did not reach statistical significance ($n = 10$, $r = 0.41$, $p = 0.07$). In contrast, there was a prominent delay in the optical signal in the CA1 relative to the CA3 (see Figure 3A). For slices in which the CA1 was present in the imaging window, there was a significant correlation between distance into CA1 and the delay in the optical signal ($n = 16$, $r = 0.52$, $p < 0.05$), with an average delay relative to the signal in CA3b of 0.4 radians (21.4 degrees; 4.3 ms) per 100 μm (Figure 3C). This is an order of magnitude greater than the mean delay of approximately 0.03 radians (1.6 degrees; 0.23 ms) per 100 μm observed within CA3. These data are consistent with propagation of the fast network oscillations along the Schaffer collaterals from CA3 into CA1, consistent with the properties of intrahippocampal gamma oscillations recorded in vivo (Csicsvari et al., 2003).

It was perhaps unexpected that no active current sinks/sources were observed in the stratum radiatum during fast network oscillations. To confirm that VSD imaging could detect a synaptically driven change of membrane potential in the dendritic membrane, we recorded the response of the CA3 network to extracellular stimulation in the stratum radiatum. This produced a transient sink in the CA3 stratum pyramidale, most likely due to antidromic conduction of action potentials into pyramidal cell somata, followed by a predominant sink/source pair in the stratum radiatum/stratum pyramidale due to local dendritic synaptic excitation (Figures 4Ai–4Ci). Indeed, VSD imaging showed that the current sink produced in the stratum radiatum by extracellular stimulation was followed by dendritic depolarization, as expected (Figure 4Di). In contrast, the current sink in the stratum radiatum during fast network oscillations was followed by membrane hyperpolarization in both the stratum pyramidale and stratum radiatum (Figures 4Aii–4Dii), suggesting that the extracellularly recorded sinks in the stratum radiatum during fast network oscillations are passive and predominantly reflect perisomatic inhibition. This result emphasizes the advantage of combining CSD analysis with other techniques to interpret CSD profiles (Bragin et al., 1995; Csicsvari et al., 2003).

Pyramidal Neurons Fire Phase Locked to Fast Network Oscillations

Both CSD and VSD profiles of the hippocampus predominantly reflect the electrical events occurring in pyramidal neurons, suggesting that carbachol-induced fast network oscillations involve rhythmic polarizations of pyramidal cell somata. To confirm the presence of these cellular oscillations, whole-cell current clamp recordings were made from CA3 pyramidal neurons, in combination with multielectrode recordings of the field potential. Eight out of ten pyramidal neurons recorded showed significant phase locking of action potential fir-

depolarization (red), and current sources (blue) were followed by hyperpolarization (blue). The membrane voltage changes spread into the dendrites, but there was no apparent membrane polarization associated directly with the current sinks/sources in the distal stratum radiatum. (B) Averages of VSD signals across slices in the stratum oriens (oriens), stratum pyramidale (pyr), proximal and distal stratum radiatum (p. rad and d. rad, respectively), and stratum lacunosum-moleculare (lm). The signals were normalized to those recorded in the distal stratum radiatum. The bilinearly interpolated, average, normalized VSD signal is presented, with the average peak-to-peak field oscillation in the distal stratum radiatum shown for reference. (Bi) The largest amplitude VSD signal was consistently observed in the stratum pyramidale, with the amplitude gradually decreasing with distance into the dendritic layers. (Bii) Maximum slopes of the VSD signal measured relative to the peak electrophysiological signal in the distal stratum radiatum. The maximum increase in the VSD signal in the stratum pyramidale occurred very shortly after the peak distal stratum radiatum field potential and after a delay in the dendritic layers. The VSD signal in the stratum lacunosum-moleculare sometimes occurred prior to that in the distal stratum radiatum, but was highly variable even after normalization. (Biii) Maximum negative slope of the VSD signal also occurred initially in the stratum pyramidale and later in the dendritic layers, but the signal in the stratum lacunosum-moleculare was more consistent with passive spread of the membrane potential changes. ($n = 25$; *$p < 0.05$; **$p < 0.01$; ***$p < 0.001$ in comparison with distal stratum radiatum; RM ANOVA, followed by within-subjects contrasts).

(C) Delay in the maximum negative slope of the VSD signal normalized to the delay at a central point in CA3b. On average, there was a significant linear delay in the VSD signal from CA3a to CA3c, and a linear fit is plotted with a lag of 0.6 radians across approximately 2 mm. Where possible, the delays in the VSD signals in the CA1 relative to the same signal in CA3b were also measured, showing a linearly increasing lag of 0.4 radians per 100 μm. For each slice, the delays were measured at equidistant points around the CA3, and the average distance between these points is given.

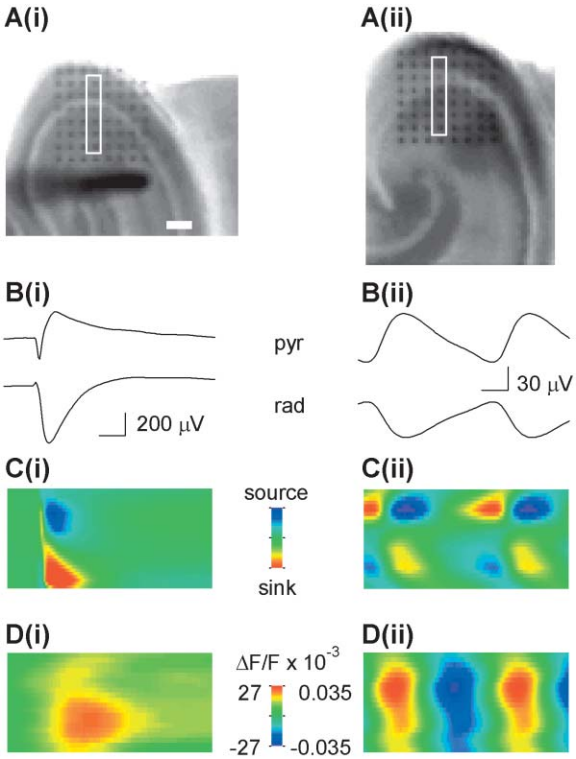

Figure 4. Comparison of the Active Sinks and Sources in CA3 Produced by Antidromic Activation and Fast Network Oscillations

(A) Multielectrode arrays were used to record field potentials in CA3 for (Ai) antidromic stimulation of the Schaffer collateral pathway and (Aii) carbachol-induced fast network oscillations. Scale bar, 200 μm. The white boxes show the electrodes used to construct 1D CSD profiles and the regions used for VSD images.

(B)(Bi) Sample averages of 16 responses evoked by bipolar stimulation (stimulation strength, 4 V) from the stratum pyramidale (pyr) and distal stratum radiatum (rad). Stimulation artifacts are removed for clarity. (Bii) Peak-to-peak cycle averages for the fast network oscillation for the stratum pyramidale and distal stratum radiatum. Horizontal scale bar, 10 ms.

(C) 1D CSD profiles were constructed for both (Ci) evoked responses and (Cii) fast network oscillations. The CSD profiles were aligned on the time of the maximum current sink (red) in the stratum radiatum, and the graphs in (B) and (D) aligned accordingly.

(D)(Di) The evoked sink in the distal stratum radiatum, accompanied by a source in the stratum pyramidale, produced a predominant depolarization in the dendritic layers. (Dii) A similar sink/source pair appearing during fast network oscillations was accompanied by a hyperpolarization of the pyramidal cell layer. The active current is the sink in the stratum radiatum for stimulation and the source in the stratum pyramidale for cholinergically induced fast network oscillations.

ing to the ongoing fast network oscillation (Rayleigh test, $p < 0.05$; spikelets were not observed). These phase locked pyramidal cells showed an average firing rate of 0.57 ± 0.18 Hz (coefficient of variation in interspike interval [CV_{ISI}] = 1.04 ± 0.17; n = 8), with a population mean phase of 5.9 [5.6, 0.1] radians (338.9 [321.6, 3.2] degrees) (second-order circular mean [95% confidence limits]) relative to the positive peak of the field oscillation in the distal stratum radiatum (Figure 5). The maximum discharge probability occurred later in the fast network oscillation, at a mean phase of 0.0 [6.0, 0.2] radians (358.2 [343.8, 12.7] degrees) (circular mean of the mode [95% confidence limits]). Such a skewed distribution of firing probability is consistent with the firing rate of the pyramidal cell population increasing as the current sink in the stratum pyramidale develops and promptly shutting off as the current source is initiated (see Figures 5D and 5F). To explore the membrane polarizations underlying these discharge probabilities, cycle averages of the pyramidal membrane potentials were constructed, excluding periods containing action potentials and the following two cycles (Figures 5D and 5E). The membrane potential was found to closely follow the field oscillation in the stratum pyramidale, with a mean delay in the peak membrane potential of 0.3 radians (14.6 degrees) (Figure 5G). Thus, both the discharge probabilities and membrane potential oscillations of CA3 pyramidal neurons are consistent with the network events suggested by the combination of CSD and VSD analysis.

Perisomatic-Targeting Interneurons Fire after Pyramidal Neurons during Fast Network Oscillations

The most likely explanation for the active source in the stratum pyramidale during fast network oscillations, accompanied by hyperpolarization of pyramidal cells and a rapid curtailment of their discharge rate, is rhythmic perisomatic inhibition. To test this hypothesis more directly, extracellular unit recordings were obtained from perisomatic-targeting interneurons in the CA3, which were subsequently intracellularly labeled for post hoc anatomical identification (Figure 6A). Five out of six perisomatic-targeting interneurons recorded participated in fast network oscillations, as evidenced by significant phase locking of action potential firing (Rayleigh test, $p < 0.05$). These interneurons fired at an average rate of 8.2 ± 2.6 Hz (CV_{ISI} = 0.72 ± 0.07; n = 5). The perisomatic-targeting interneurons fired at a significantly later phase in the oscillation than did the pyramidal neurons, with a mean phase of 0.6 [0.0, 1.7] radians (34.0 [2.4, 97.1] degrees) (two-sample Hotelling test; $F_{2,10} = 44.5$, $p < 0.001$ compared with phase-locked pyramidal cells) and a mean phase of maximum discharge probability at 0.5 [0.2, 0.9] radians (30.1 [11.4, 48.8] degrees) (Watson-Williams test; $F_{1,11} = 10.3$, $p < 0.01$ compared with phase locked pyramidal cells) (Figures 6B–6E). For a fast network oscillation at 20 Hz, these phase delays between the firing of pyramidal neurons and perisomatic-targeting interneurons correspond to time delays of 7.7 ms and 4.4 ms for the average mean and mode discharge phases, respectively. These values would be consistent with monosynaptic excitation of perisomatic inhibitory cells by pyramidal neurons.

Fast Synaptic Excitation and Inhibition Are Both Necessary for Oscillogenesis

All of these results indicate a major role for chemical synaptic transmission in cholinergically induced gamma activity. We therefore proceeded with a pharmacological dissection of the synaptic currents involved. Bath application of AMPA (α-amino-3-hydroxy-5-methyl-4-isoxazolepropionic acid) receptor-selective antagonist GYKI 53655 (10–25 μM) (Tarnawa et al., 1993; Bleakman et al., 1996) completely blocked carbachol-induced oscillations (power in the 10–45 Hz band; 174.9 ± 35.8 versus

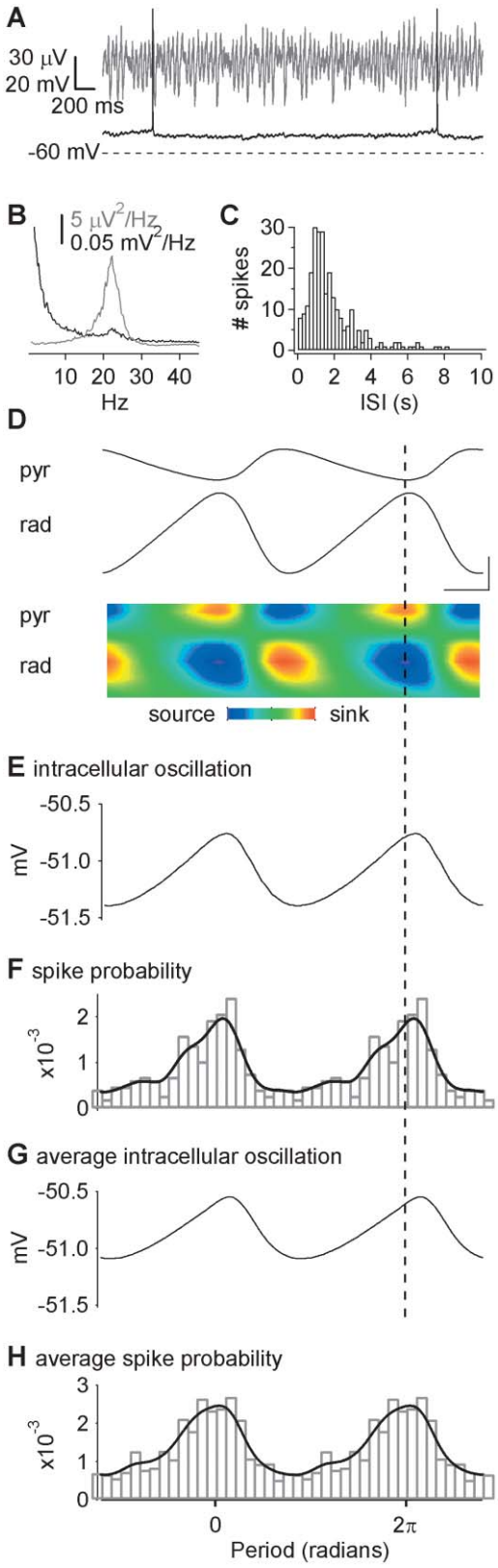

Figure 5. Pyramidal Cell Discharge and Intracellular Oscillations during Fast Network Oscillations

Multielectrode arrays were used to record field potentials in CA3 during carbachol-induced fast network oscillations, with simultaneous recording in whole-cell current-clamp from identified CA3 pyramidal cells. (A) Typical activity recorded from a CA3 pyramidal neuron (black trace) during carbachol-induced oscillations, showing low-frequency single action potential firing. The intracellular recording is aligned with the field potential recorded in the distal stratum radiatum (gray trace). Action potentials are truncated at +30 mV. (B) Power spectral density of the intracellular oscillation of the recorded pyramidal neuron (black) and the field oscillation in the distal stratum radiatum (gray), both showing peaks at ~20 Hz. (C) Interspike interval histogram for the recorded pyramidal neuron. (D) Peak-to-peak cycle averages of the field recordings from the stratum pyramidale (pyr) and distal stratum radiatum (rad) during the carbachol-induced fast network oscillation shown in (A), with the 1D CSD profile below. The vertical dashed line shows the time of the peak sink in the stratum pyramidale. Scale bars, 10 μV and 10 ms. (E) Cycle average of the membrane potential of a pyramidal cell recorded during the network oscillation shown in (A), with the exclusion of periods containing spikes or spike afterhyperpolarizations. The membrane potential peaked after the maximum sink in the stratum pyramidale, with a delay of 0.3 radians. (F) Spike probability histogram for the pyramidal cell, with the estimated probability density function superimposed. The profile of pyramidal cell discharge was skewed, with a mean phase of 6.1 radians relative to the peak signal recorded in the distal stratum radiatum. The peak discharge probability at 0.1 radians, measured from the estimated probability density function, coincided with the peak in the intracellular membrane potential oscillation in the absence of firing shown in (E). (G) The average intracellular membrane oscillation for the eight out of ten pyramidal cells that showed significant phase coupling to the fast network oscillations. Confidence limits have been omitted for clarity. (H) The average spike probability histogram and estimated probability density function for phase-coupled pyramidal cells (n = 8).

5.4 ± 2.5 μV^2; paired two-sample t test on log power; $p < 0.001$, n = 8), while the NMDA (*N*-methyl-D-aspartate) receptor antagonist D-AP5 (50 μM) had no significant effect (285.1 ± 113.1 versus 214.6 ± 70.9 μV^2; n = 4). The $GABA_A$ (γ-aminobutyric acid) receptor antagonist gabazine (200 nM) blocked carbachol-induced oscillations (57.8 ± 13.2 versus 3.8 ± 1.0 μV^2; $p < 0.01$, n = 4) and induced ripple-associated epileptiform events at higher concentrations (see Supplemental Figure S2) [http://www.neuron.org/cgi/content/full/45/1/105/DC1/]). The $GABA_B$ receptor antagonist CGP 52432 (5 μM) had no significant effect (215.6 ± 62.4 versus 209.0 ± 53.8 μV^2; n = 4). Therefore, consistent with previous reports, carbachol-induced oscillations appear to be dependent upon fast GABAergic inhibition and AMPA receptor-mediated excitation (Fisahn et al., 1998).

Fast Synaptic Transmission in the Stratum Radiatum Is Not Required for Oscillogenesis

The apical dendrites of pyramidal neurons receive recurrent excitation and feedback inhibition, so how do these dendritic currents contribute to oscillogenesis and the generation of the field potential? This question was addressed through local blockade of synaptic transmission in the strata radiatum and lacunosum-moleculare. The efficacy of local antagonist application was assessed by the effects on responses to extracellular stimulation in the stratum radiatum. Local application of 12.5 mM GYKI 53655 reduced the negative peak of the fEPSP across the stratum radiatum by 95% ± 2%, yet subsequent bath application of 25 μM carbachol still induced fast network oscillations (16.1 ± 0.9 Hz; n = 3; Figure 7A). Further perisomatic application of GYKI 53655 blocked

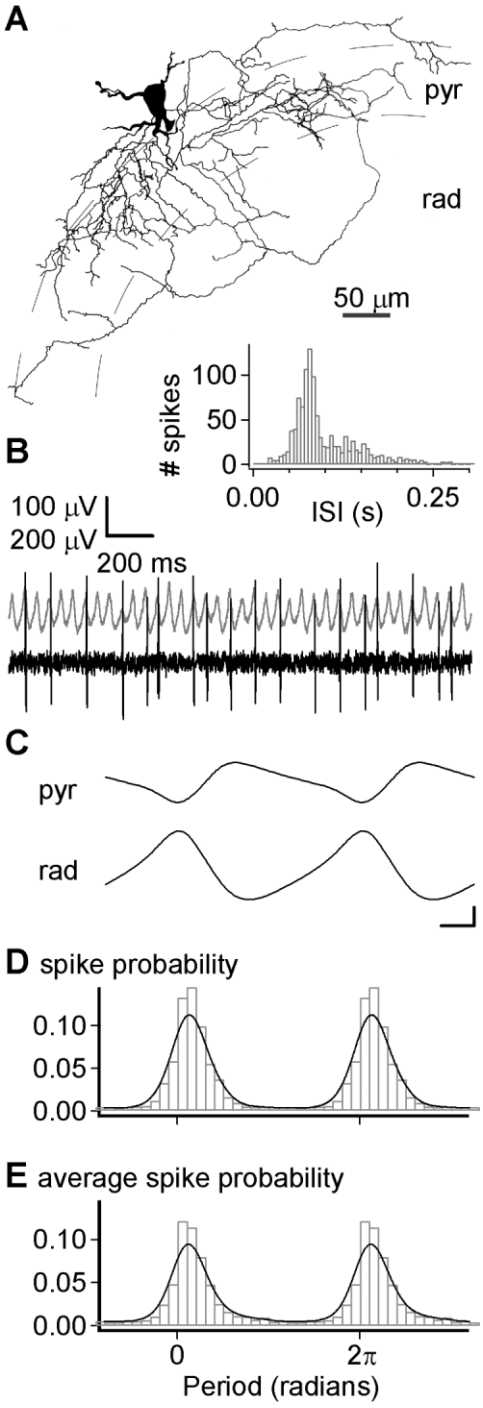

Figure 6. Discharge Probabilities of Perisomatic-Targeting Interneurons Relative to Fast Network Oscillations

Single-unit activity from visually identified interneurons in CA3 were recorded simultaneously with multielectrode recordings of the fast network oscillations. The interneurons were subsequently labeled for morphological identification, and only those showing axon arborization in the perisomatic regions of CA3 pyramidal neurons were included in the analysis. (A) Reconstruction of a perisomatic-targeting interneuron in the CA3, recorded during carbachol-induced fast network oscillations. Dashed gray lines represent the borders of the stratum pyramidale (pyr). rad, stratum radiatum. Scale bar, 50 μm. (B) Unit recording from interneuron shown in (A) (high-pass filtered at 200 Hz), aligned with field recording from the distal stratum radiatum. (Inset) Interspike interval histogram. (C) Peak-to-peak cycle averages for the field recordings from the stratum pyramidale (pyr) and distal stratum radiatum (rad) during the fast network oscillation in which cell (A) was recorded. Scale bars, 20 μV and 10 ms. (D) Spike probability histogram for the perisomatic-targeting interneuron shown in (A), with superimposed estimated probability density function. (E) The average spike probability histogram and estimated probability density function for phase-coupled perisomatic-targeting interneurons (n = 5).

these oscillations (power in the 10–45 Hz band; 160.5 ± 141.7 versus 1.5 ± 0.4 μV^2; paired two-sample t test on log power; $p < 0.05$, $n = 3$). Local application of 100 μM gabazine in the stratum radiatum increased the negative peak of the fEPSP by 33% ± 6% ($n = 5$), which appeared to represent near-maximum blockade of local phasic inhibition; additional application of carbachol induced fast network oscillations in 3 out of 5 slices (19.5 ± 2.8 Hz; Figure 7A) and large-amplitude (~3 Hz) epileptiform discharges in the other two slices. The fast network oscillations were blocked by further perisomatic application of gabazine (77.2 ± 25.6 versus 4.9 ± 1.7 μV^2; $p < 0.05$, $n = 3$) (Figure 7A).

These results suggest that synaptic inputs to the apical dendrites of pyramidal neurons are not necessary for oscillogenesis. Indeed, local application of 1 mM tetrodotoxin (TTX), which reduced the negative peak of the fEPSP by 97% ± 1%, did not prevent the subsequent induction of network oscillations (12.5 ± 2.7 Hz; power area in 5–45 Hz band, 51.2 ± 14.5 μV^2; $n = 3$; Figure 7A). However, these oscillations appeared to have slightly different properties from those recorded under control conditions, and, to further investigate such effects, TTX was applied in the strata radiatum and lacunosum-moleculare after oscillations had been induced. It was found that local application of TTX significantly reduced the oscillation frequency (16.1 ± 1.9 versus 10.5 ± 1.4 Hz; paired two-sample t test; $p < 0.05$, $n = 5$) and changed the waveform (Figures 7B and 7C; see Supplemental Figure S3 for details [http://www.neuron.org/cgi/content/full/45/1/105/DC1/]), but the oscillations remained associated with alternating sink and source pairs in the stratum pyramidale and distal stratum radiatum (Figure 7D). In one experiment, it was confirmed that additional perisomatic application of TTX abolished all oscillatory activity. Therefore, currents in the stratum radiatum/lacunosum-moleculare appear to elaborate the principal oscillatory events at perisomatic sites.

Fast Synaptic Excitation of Both Pyramidal Neurons and Interneurons Is Necessary for Beta-Gamma Frequency Rhythmic Inhibition

Finally, in order to examine the precise function of fast synaptic excitation in oscillogenesis, we recorded from individual pyramidal cells and perisomatic-targeting interneurons during the application of a selective AMPA receptor antagonist, GYKI 53655. This treatment blocked carbachol-induced oscillations (as shown earlier) and was accompanied by a hyperpolarization of pyramidal cells below action potential threshold (12.5 μM GYKI 53655; membrane potential, −59.6 ± 3.1 versus −67.2 ± 1.8 mV; firing rate, 0.42 ± 0.20 versus 0 Hz; $n = 4$;

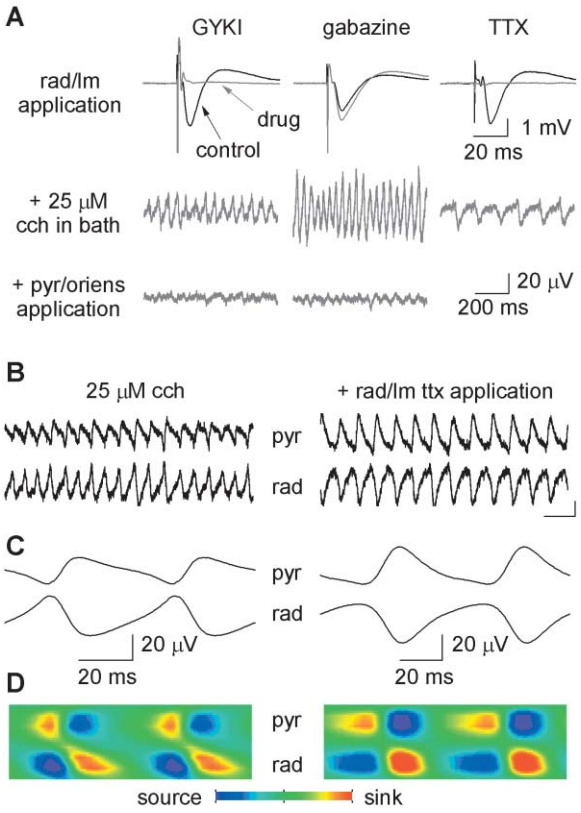

Figure 7. Synaptic Transmission in the Strata Radiatum and Lacunosum-Moleculare Is Not Required for Oscillogenesis

(A) Multielectrode arrays were used to record field potentials across the CA3, with representative traces from single electrodes in the stratum radiatum displayed. Initially, responses to antidromic stimulation of the Schaffer collateral pathway were recorded to monitor the effects of local pressure ejection in the strata radiatum and lacunosum-moleculare of the AMPA receptor-selective antagonist GYKI 53655 (GYKI, 12.5 mM), the $GABA_A$ receptor antagonist gabazine (100 μM), or tetrodotoxin (TTX, 1 mM). For GYKI and TTX experiments, application continued until the fEPSP disappeared, while gabazine was applied until the negative peak of the fEPSP increased by ~30%. Subsequent bath application of 25 μM carbachol (CCh) was still able to induce network oscillations. Further local application of GYKI and gabazine in the strata pyramidale and oriens abolished the oscillations.

(B) The effects of local application of TTX (1 mM) in the strata radiatum and lacunosum-moleculare on previously established carbachol-induced fast network oscillations recorded in the stratum pyramidale (pyr) and distal stratum radiatum (rad), showing a reduction in oscillation frequency and a change in waveform. Scale bars, 20 μV and 100 ms.

(C) Peak-to-peak cycle averages for the oscillations recorded in the stratum pyramidale and distal stratum radiatum.

(D) The 1D CSD profiles for carbachol-induced oscillations before and after local application of TTX in the strata radiatum and lacunosum-moleculare displayed alternating current sink (red) and source (blue) pairs in the stratum pyramidale and stratum radiatum.

Figure 8A). This suggests that AMPA receptor-mediated excitation contributes to the depolarization of pyramidal cells, but does not resolve the role of such fast excitation in network synchronization. As blocking AMPA receptors shifts the membrane potential of pyramidal cells toward the reversal potential for $GABA_A$ receptors, it is conceivable that a network of interneurons could still fire synchronously, but elicit reduced synaptic currents, thus rendering this oscillation undetectable in the field potential. To evaluate the effect of GYKI 53655 on synchronized inhibition, we recorded excitatory and inhibitory postsynaptic currents (EPSCs and IPSCs) in CA3 pyramidal cells held in whole-cell voltage clamp at −70 mV and 0 mV, respectively. We found that, in addition to completely blocking the fast network oscillations recorded in the field potential (power in the 10–45 Hz band; 227.6 ± 58.2 versus 2.5 ± 1.5 μV^2; paired two-sample t test on log power; $p < 0.01$, $n = 4$), 10–25 μM GYKI 53655 blocked both EPSCs (131.1 ± 66.8 versus 2.5 ± 0.6 pA^2; $p < 0.01$, $n = 4$) and rhythmic IPSCs (520.9 ± 200.7 versus 26.8 ± 10.8 pA^2; $p < 0.01$, $n = 4$) (Figures 8B–8D). Therefore, fast synaptic excitation appears to be necessary for interneuronal synchronization.

To test whether such AMPA receptor-mediated excitation is also required for the recruitment of inhibition, extracellular unit recordings were obtained from five anatomically identified perisomatic-targeting interneurons. Application of 10–25 μM GYKI 53655 had no significant effect on firing rate (8.8 ± 1.1 versus 7.3 ± 1.2 Hz; paired t test, $n = 5$) (Figure 8E), demonstrating that these interneurons can fire independently of fast synaptic excitation. However, the initial degree of phase coupling appeared to be positively correlated with the extent to which AMPA receptor-mediated excitation determined this interneuronal firing pattern, as measured by the effect of GYKI 53655 on both the ISI mean ($n = 5$, $r = 0.66$, not significant) and ISI mode ($n = 5$, $r = 0.65$, not significant) (Figures 8F–8H). These results support the proposition that cholinergically induced fast network oscillations are dependent upon fast synaptic excitation to both maintain the excitability of pyramidal neurons and synchronize the firing of perisomatic-targeting GABAergic interneurons.

Discussion

Our principal findings are that (1) cholinergically induced fast network oscillations in the hippocampus in vitro are associated with alternating current sink and source pairs in the CA3 stratum pyramidale and stratum radiatum, which resemble those observed during intrahippocampal gamma oscillations in vivo, (2) the active current sinks and sources are localized in the stratum pyramidale, as revealed by voltage-sensitive dye imaging, local blockade of synaptic transmission, and intracellular recordings from CA3 pyramidal cells, (3) these oscillations are driven by rhythmic hyperpolarizing GABAergic inputs to pyramidal cells from perisomatic-targeting interneurons, and (4) the synchronization of the perisomatic-targeting interneurons and, thus, the generation of fast network oscillations are dependent on AMPA receptor-mediated fast recurrent excitation from pyramidal cells.

Both 1D and 2D CSD analysis revealed that cholinergically induced fast network oscillations in the CA3 are associated with alternating current sink and source pairs in the strata pyramidale and radiatum (Figure 2), which is similar to the sink/source distribution observed during intrahippocampal gamma oscillations in the behaving rat (Bragin et al., 1995; Csicsvari et al., 2003). Indeed, this

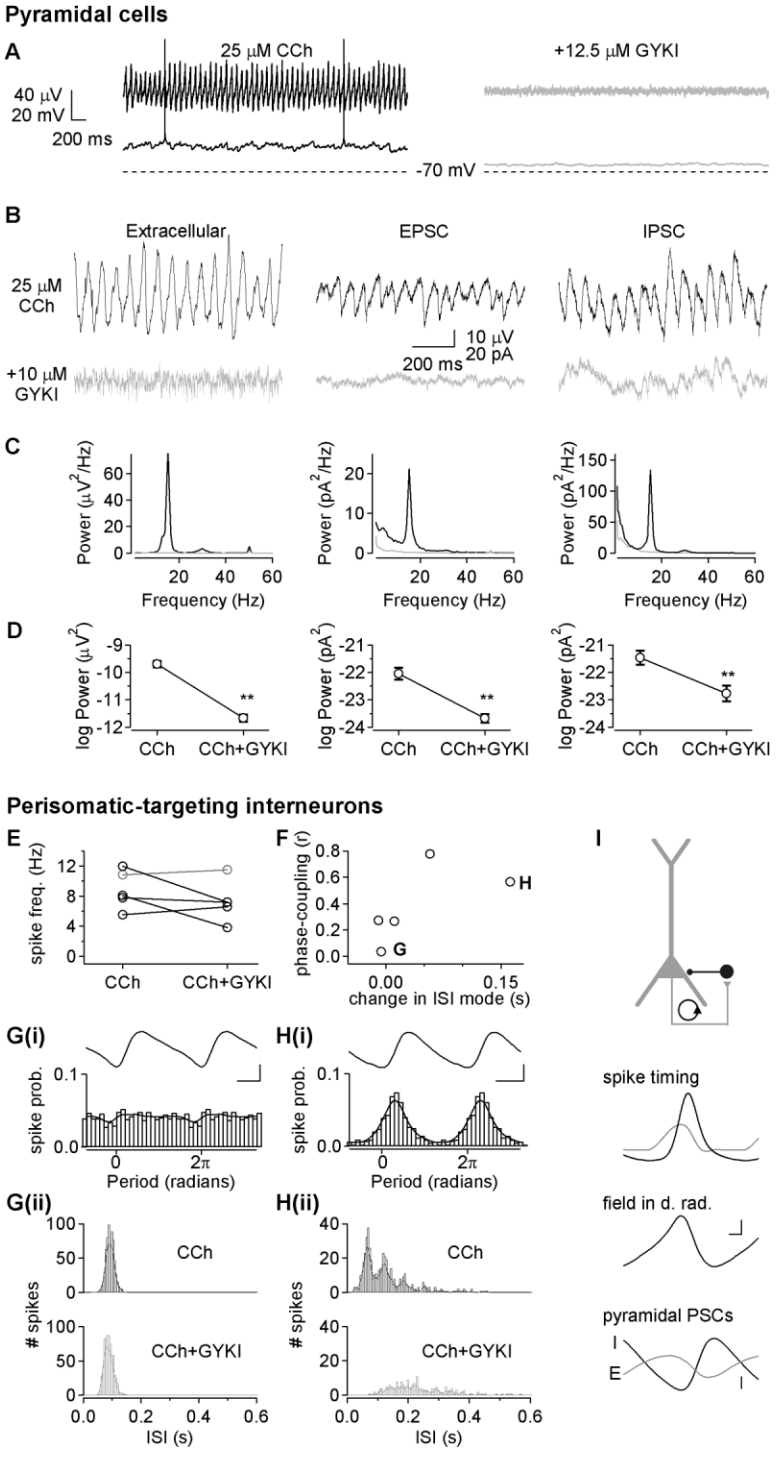

Figure 8. Carbachol-Induced Oscillations Are Dependent on Fast Synaptic Transmission

(A) Whole-cell current-clamp from CA3 pyramidal cells was performed simultaneously with multielectrode recordings of the fast network oscillation. Application of the AMPA receptor-selective antagonist GYKI 53655 (GYKI) blocked the extracellular field oscillations and produced a hyperpolarization of pyramidal neurons below action potential threshold (n = 4). Action potentials are truncated at +20 mV.

(B) In separate experiments, synaptic currents recorded in whole-cell voltage-clamp from CA3 pyramidal neurons at holding potentials of −70 mV (EPSC) and 0 mV (IPSC) were monitored simultaneously with multielectrode recordings of the fast network oscillation. Extracellular field oscillations (example from the distal stratum radiatum of CA3) and both rhythmic EPSCs and IPSCs were blocked by GYKI 53655.

(C) Power spectral density plots for the recordings from field, EPSCs, and IPSCs in the presence of 25 μM carbachol (black lines). In some cases there was also a low-frequency peak in the power spectral density of the EPSC recording. Following the application of GYKI 53655, the oscillatory components of both field potential and synaptic currents disappeared (gray lines).

(D) Logarithm of the power in the 10–45 Hz range plotted for the statistical analysis of the average effects of GYKI 53655 (10–25 μM) on the fast network oscillations induced by 25 μM carbachol (CCh). (n = 4, **$p < 0.01$; paired two-sample t test.)

(E) Application of 10–25 μM GYKI 53655 had no significant effect on the firing rate of anatomically identified perisomatic-targeting interneurons (n = 5, $p > 0.05$; paired two-sample t test; black markers). The cell depicted in gray was not significantly phase coupled (Rayleigh test, $p > 0.05$).

(F) The phase coupling of the perisomatic-targeting interneurons to the network oscillation, as measured by the vector length (r), was positively correlated with the subsequent effect of 10–25 μM GYKI 53655 on the ISI mode. Cells analyzed in more detail in panels (G) and (H) are labeled.

(G)(Gi) Peak-to-peak cycle averages for the field recordings from the stratum pyramidale during the fast network oscillation in which the non-phase-coupled perisomatic-targeting interneuron was recorded. Below is the spike probability histogram, with superimposed estimated probability density function. Scale bars, 40 μV and 20 ms. (Gii) Interspike interval histogram before (black) and after (gray) GYKI 53655 application, showing that the firing of this non-phase-coupled perisomatic-targetinginterneuron was not controlled by AMPA receptor-mediated excitation.

(H) Same analysis as in panel (G) for a perisomatic-targeting interneuron that was strongly phase-coupled, showing that fast excitation contributes to driving the firing of some interneurons, in addition to its role in synchronization. Scale bars, 40 μV and 20 ms.

(I) Synaptic feedback model for the generation of fast network oscillations in vitro, involving primarily CA3 pyramidal neurons (gray) and perisomatic-targeting interneurons (black). Below the cartoon are the average estimated probability density functions for the spiking of pyramidal cells (gray) and interneurons (black). To facilitate comparison, the functions have been normalized to an area of 1 prior to averaging. The cycle average of the oscillations in the distal stratum radiatum (d. rad.) is shown below (experiments in [B]–[D]) (scale bars, 10 μV and π/8 radians). The bottom figure depicts the corresponding average inhibitory (I) and excitatory (E) postsynaptic currents (PSCs) recorded in pyramidal neurons during fast network oscillations. (n = 4; scale bar, 10 pA.)

in vitro model shares many physiological characteristics with hippocampal gamma oscillations in vivo. In particular, pyramidal neurons fire at low frequencies (<5 Hz), phase locked to the current sink in stratum pyramidale (Figure 5) (Penttonen et al., 1998; Csicsvari et al., 2003); the pyramidal neurons receive rhythmic inhibition (Penttonen et al., 1998) (Figure 6); and perisomatic-targeting interneurons in the CA3 are capable of firing on almost every cycle of the oscillation, but discharge at a significantly later phase than do CA3 pyramidal cells (see Figures 5, 6, and 8I) (Csicsvari et al., 2003). Furthermore, in both cases the oscillation appears to be generated in CA3 and propagate to CA1 (Figure 3C) (Fisahn et al., 1998; Csicsvari et al., 2003).

The advantage of using an in vitro model of hippocampal gamma oscillations was that we could use a combination of different techniques to examine more directly the cellular and network mechanisms underlying "current" and "rhythm" generation, i.e., the cellular currents that generate the oscillation in the extracellular field potential and the mechanism by which such activity is synchronized. First, a comparison of 1D and 2D CSD analyses showed only subtle differences between them in the magnitude of the currents, temporal relations, and the precise localization of phase reversal (Figure 2 and Supplemental Figure S1 [http://www.neuron.org/cgi/content/full/45/1/105/DC1/]), justifying the use of 1D CSD for fast oscillations in vivo. Second, VSD imaging (Grinvald et al., 1982; Tominaga et al., 2002) was employed to identify the active sinks and sources during fast network oscillations. The dye signal has been shown earlier to reflect predominantly the membrane polarizations of pyramidal neurons (Tominaga et al., 2000). This signal occurred first and with the largest amplitude in the pyramidal cell layer, suggesting a perisomatic origin of sinks and sources (Figure 3). This result was supported by intracellular recordings from CA3 pyramidal neurons (Figure 5) and the fact that blocking synaptic transmission in the strata radiatum and lacunosum-moleculare did not prevent oscillogenesis (Figure 7). Together, these results demonstrate that cholinergically induced fast oscillations in the field potential primarily reflect rhythmic currents at the level of pyramidal cell somata and perisomatic membrane, rather than distal dendritic excitation or inhibition.

Although pyramidal cells receive rhythmic excitation (Figure 8B), an active current sink was not detected in the stratum radiatum (Figures 3, 4, and 7), probably because recurrent excitation has a relatively small amplitude and/or targets both the apical and basal dendrites. In fact, it has been reported that the majority of boutons from pyramidal cells in CA3 are found in the stratum oriens (Sik et al., 1993). Thus, it is likely that much of the synaptic excitation occurs in the basal dendrites. This recurrent excitation is important for the depolarization of pyramidal neurons (Figure 8A) in conjunction with intrinsic tonic conductances (Fisahn et al., 2002), which might explain why carbachol-induced fast network oscillations are generated in the CA3 and not in the CA1 (Figure 3; Fisahn et al., 1998).

Evidence from both in vitro and in vivo studies supports the hypothesis that fast network oscillations are driven by perisomatic inhibition (Figure 6) (Whittington et al., 1995; Fisahn et al., 1998; Penttonen et al., 1998; Traub et al., 2000; Csicsvari et al., 2003), but does not resolve the question of how these interneurons would be synchronized. In this study, we showed that an AMPA receptor-selective antagonist (10–25 μM GYKI 53655) blocked both the field oscillation and rhythmic inhibitory currents on pyramidal neurons (Figure 8), suggesting that interneuronal synchronization is mediated by fast recurrent excitation. Therefore, cholinergically induced fast network oscillations in the CA3 appear to be generated by a synaptic feedback circuit between pyramidal cells and perisomatic-targeting interneurons (Figure 8I), consistent with the model originally suggested for prepyriform cortex by Freeman (1968).

Studying the mechanisms of hippocampal gamma oscillations in a cholinergic model appears relevant, since the dense cholinergic projection to the hippocampus, originating from the medial septum/diagonal band of Broca, is thought to play a permissive role in the generation of hippocampal network oscillations (Leung, 1985; but see Lee et al., 1994). Nonetheless, fast network oscillations in the hippocampus in vitro can be induced by a variety of paradigms (for review, see Whittington and Traub, 2003), which might recruit additional mechanisms contributing to network synchronization, such as interneuronal (Whittington et al., 1995) or axo-axonal coupling (Traub et al., 2001, 2003a, 2003b; Fischer, 2004) via gap junctions. Gap junction blockers, such as carbenoxolone and octanol, block gamma frequency oscillations in vitro (Traub et al., 2000), but these drugs may have other effects that can inhibit network activity via different mechanisms (Rouach et al., 2003; Fischer, 2004; Vessey et al., 2004). Indeed, mice deficient in connexin36, the predominant neuronal gap junction protein in the brain (Rash et al., 2000), continue to display gamma oscillations both in vitro (Hormuzdi et al., 2001) and in vivo (Buhl et al., 2003), although the power of these oscillations is substantially reduced. Chemical synaptic interactions are sufficient for fast synchronization in network models of leaky integrate-and-fire neurons with physiologically realistic firing rates (Brunel and Wang, 2003), and, overall, the CA3 synaptic feedback model appears to explain satisfactorily the generation of both cholinergically induced fast network oscillations in vitro (Figure 8) (Fisahn et al., 1998) and intrahippocampal gamma oscillations in vivo (Csicsvari et al., 2003). Gap junction coupling might play a more fundamental role in the generation of gamma oscillations in other subregions of the hippocampus (Traub et al., 2003a).

Elucidating the mechanisms underlying current and rhythm generation of intrahippocampal gamma oscillations is necessary in order to understand both how individual cell types process the collective network input and also identify the functional processes that this rhythm could support. With its predominantly perisomatic location, the source of hippocampal gamma oscillations appears to control primarily the output of hippocampal pyramidal neurons. Such a mechanism might permit the dendritic integration of inputs that are not phase coupled to the intrahippocampal oscillation. Furthermore, since gamma frequency rhythmic inhibition appears to be synchronized by the firing of the pyramidal neurons themselves, hippocampal gamma oscillations could enable the serial activation and disbandment of

neuronal assemblies and thus support the encoding and retrieval of memory sequences.

Experimental Procedures

Slice Preparation and Electrophysiology

Detailed methods are provided in the Supplemental Data (http://www.neuron.org/cgi/content/full/45/1/105/DC1/). Briefly, horizontal hippocampal slices (400 μm) were prepared from P12–P18 Wistar rats and maintained in an interface chamber, between humidified carbogen gas (95% O_2/5% CO_2) and artificial cerebrospinal fluid (ACSF) containing 126 mM NaCl, 3 mM KCl, 1.25 mM NaH_2PO_4, 2 mM $MgSO_4$, 2 mM $CaCl_2$, 26 mM $NaHCO_3$, and 10 mM glucose (pH 7.2–7.4). Slices were left to recover at room temperature for at least 1 hr. For recordings, slices were mounted on 8 × 8 arrays of planar microelectrodes (electrode size, 20 μm × 20 μm; interpolar distance, 100 μm; Panasonic MED-P2105; Tensor Biosciences, Irvine, CA), maintained in a submerged condition at room temperature, and superfused with ACSF, bubbled with carbogen, at 3–6 ml/min^{-1}. Electrical stimuli (0.02 ms square pulse) were delivered through a concentric bipolar electrode (FHC, Bowdoinham, ME) controlled via a stimulation isolation unit (Digitimer, Welwyn Garden City, UK). Spontaneous and evoked field potentials from all 64 recording electrodes were acquired simultaneously at 2–5 kHz, using the Panasonic MED64 system (Tensor Biosciences).

For voltage-sensitive dye imaging, each slice was stained for 25 min with VSD solution, containing 200 μM Di-4-ANEPPS (Molecular Probes) in 2.7% ethanol, 0.13% Cremaphor EL (Sigma), 50% fetal bovine serum (Sigma), and 50% ACSF. Optical signals were recorded using a MiCAM01 CCD camera (BrainVision; SciMedia Ltd., Tokyo, Japan), with a spatial resolution of approximately 22 × 22 μm and an acquisition rate of 200–500 Hz.

Whole-cell current-clamp recordings from CA3 pyramidal neurons were performed with glass pipettes, pulled from standard borosilicate glass, containing: 110 mM potassium gluconate, 40 mM HEPES, 4 mM NaCl, 2 mM ATP-Mg, 0.3 mM GTP, and 5 mg/ml^{-1} biocytin (pH 7.2–7.3; osmolarity, 290–300 mosmol/l^{-1}). For whole-cell voltage-clamp recordings, potassium gluconate was replaced with equimolar cesium gluconate. Single-unit recordings from interneurons were made with patch pipettes filled with ACSF and were performed to avoid altering the intracellular milieu, which affects action potential timing in interneurons (N.H., unpublished data). Current-clamp and single-unit recordings were made with an Axoclamp-2B amplifier in bridge mode, while voltage-clamp recordings were made with an Axopatch-1D amplifier. Following intracellular recording, the slices were fixed in 4% paraformaldehyde in 0.1 M phosphate buffer (PB; pH 7.4). Biocytin-filled cells were visualized following standard procedures.

Data Analysis

CSD analysis was performed on the peak-to-peak average cycles using previously described methods (Shimono et al., 2000). CSDs are shown using an inverted color scale, with warm colors corresponding to sinks (i.e., neuronal membrane inward currents). For analysis of the optical signal, the peak-to-peak average of fractional change in fluorescence over time was passed through a 5 × 5 × 5 point averaging filter. Depolarization produces a reduction in fluorescence; thus, to allow depolarization to be represented by positive values, the polarity of the fluorescence signal was inverted.

The spike timing in single cells was analyzed relative to the ongoing field oscillation, and cells not significantly coupled to the network were excluded from further analysis (Rayleigh test, $p < 0.05$). The modal phase was determined from the estimated probability density functions. For comparisons between cell classes, the population mean mode was quantified as a first-order circular statistic (Watson-Williams test), and the population mean of the mean phases was quantified as a second-order circular statistic (Hotelling test) (Batschelet, 1981; Zar, 1999).

All data are presented as means ± SEM, except where stated. Paired Student's t tests, repeated measures analysis of variance (RM ANOVA), and Pearson correlation coefficients were calculated in SPSS. Circular statistics were programmed in Igor.

Drugs and Chemicals

GYKI 53655 was a gift from IVAX Drug Research Institute, Ltd. (Budapest, Hungary). All other drugs and chemicals were obtained from Sigma-Aldrich (Poole, Dorset, UK) and Tocris (Bristol, UK). Local application of antagonists in ACSF was achieved by pressure ejection through a patch pipette (50–200 ms; 10 psi; 30–60 applications per hippocampal subregion), using a Picospritzer II (General Valve Corporation).

Acknowledgments

The authors are grateful to Ms. Charmaine Nelson for help with histological processing. The research was supported by the Biotechnology and Biological Sciences Research Council (UK). Additional financial support from Matsushita Co., Ltd. (Japan), Alpha Med Sciences Co., Ltd. (Japan), and Pfizer, Inc. (USA) is gratefully acknowledged. N.H. was a grantee of the NATO Science Fellowship.

Received: April 30, 2004
Revised: August 5, 2004
Accepted: November 17, 2004
Published: January 5, 2005

References

Batschelet, E. (1981). Circular statistics in biology (London: Academic Press).

Bleakman, D., Ballyk, B.A., Schoepp, D.D., Palmer, A.J., Bath, C.P., Sharpe, E.F., Woolley, M.L., Bufton, H.R., Kamboj, R.K., Tarnawa, I., and Lodge, D. (1996). Activity of 2,3-benzodiazepines at native rat and recombinant human glutamate receptors in vitro: stereospecificity and selectivity profiles. Neuropharmacology *35*, 1689–1702.

Bragin, A., Jando, G., Nadasdy, Z., Hetke, J., Wise, K., and Buzsaki, G. (1995). Gamma (40–100 Hz) oscillation in the hippocampus of the behaving rat. J. Neurosci. *15*, 47–60.

Brunel, N., and Wang, X. (2003). What determines the frequency of fast network oscillations with irregular neural discharges? I. Synaptic dynamics and excitation-inhibition balance. J. Neurophysiol. *90*, 415–430.

Buhl, D.L., Harris, K.D., Hormuzdi, S.G., Monyer, H., and Buzsaki, G. (2003). Selective impairment of hippocampal gamma oscillations in connexin-36 knock-out mouse in vivo. J. Neurosci. *23*, 1013–1018.

Buzsaki, G. (2002). Theta oscillations in the hippocampus. Neuron *33*, 325–340.

Buzsaki, G., Buhl, D.L., Harris, K.D., Csicsvari, J., Czeh, B., and Morozov, A. (2003). Hippocampal network patterns of activity in the mouse. Neuroscience *116*, 201–211.

Csicsvari, J., Jamieson, B., Wise, K.D., and Buzsaki, G. (2003). Mechanisms of gamma oscillations in the hippocampus of the behaving rat. Neuron *37*, 311–322.

Dickinson, R., Awaiz, S., Whittington, M.A., Lieb, W.R., and Franks, N.P. (2003). The effects of general anaesthetics on carbachol-evoked gamma oscillations in the rat hippocampus in vitro. Neuropharmacology *44*, 864–872.

Fellous, J.M., and Sejnowski, T.J. (2000). Cholinergic induction of oscillations in the hippocampal slice in the slow (0.5–2 Hz), theta (5–12 Hz), and gamma (35–70 Hz) bands. Hippocampus *10*, 187–197.

Fisahn, A., Pike, F.G., Buhl, E.H., and Paulsen, O. (1998). Cholinergic induction of network oscillations at 40 Hz in the hippocampus in vitro. Nature *394*, 186–189.

Fisahn, A., Yamada, M., Duttaroy, A., Gan, J.W., Deng, C.X., McBain, C.J., and Wess, J. (2002). Muscarinic induction of hippocampal gamma oscillations requires coupling of the M1 receptor to two mixed cation currents. Neuron *33*, 615–624.

Fischer, Y. (2004). The hippocampal intrinsic network oscillator. J. Physiol. *554*, 156–174.

Freeman, W.J. (1968). Relations between unit activity and evoked potentials in prepyriform cortex of cats. J. Neurophysiol. *31*, 337–348.

Fries, P., Neuenschwander, S., Engel, A.K., Goebel, R., and Singer, W. (2001). Rapid feature selective neuronal synchronization through correlated latency shifting. Nat. Neurosci. *4*, 194–200.

Grinvald, A., Manker, A., and Segal, M. (1982). Visualization of the spread of electrical activity in rat hippocampal slices by voltage-sensitive optical probes. J. Physiol. *333*, 269–291.

Hasselmo, M.E., Wyble, B.P., and Wallenstein, G.V. (1996). Encoding and retrieval of episodic memories: role of cholinergic and GABAergic modulation in the hippocampus. Hippocampus *6*, 693–708.

Holsheimer, J. (1987). Electrical conductivity of the hippocampal CA1 layers and application to current-source-density analysis. Exp. Brain Res. *67*, 402–410.

Hormuzdi, S.G., Pais, I., LeBeau, F.E., Towers, S.K., Rozov, A., Buhl, E.H., Whittington, M.A., and Monyer, H. (2001). Impaired electrical signaling disrupts gamma frequency oscillations in connexin 36-deficient mice. Neuron *31*, 487–495.

Jensen, O., and Lisman, J.E. (1996). Theta/gamma networks with slow NMDA channels learn sequences and encode episodic memory: role of NMDA channels in recall. Learn. Mem. *3*, 264–278.

Lee, M.G., Chrobak, J.J., Sik, A., Wiley, R.G., and Buzsaki, G. (1994). Hippocampal theta activity following selective lesion of the septal cholinergic system. Neuroscience *62*, 1033–1047.

Leung, L.W. (1985). Spectral analysis of hippocampal EEG in the freely moving rat: effects of centrally active drugs and relations to evoked potentials. Electroencephalogr. Clin. Neurophysiol. *60*, 65–77.

Lisman, J.E., and Idiart, M.A. (1995). Storage of 7 +/− 2 short-term memories in oscillatory subcycles. Science *267*, 1512–1515.

Llinas, R., Ribary, U., Contreras, D., and Pedroarena, C. (1998). The neuronal basis for consciousness. Philos. Trans. R. Soc. Lond. B Biol. Sci. *353*, 1841–1849.

Mitzdorf, U. (1985). Current source-density method and application in cat cerebral cortex: investigation of evoked potentials and EEG phenomena. Physiol. Rev. *65*, 37–100.

Oka, H., Shimono, K., Ogawa, R., Sugihara, H., and Taketani, M. (1999). A new planar multielectrode array for extracellular recording: application to hippocampal acute slice. J. Neurosci. Methods *93*, 61–67.

Penttonen, M., Kamondi, A., Acsady, L., and Buzsaki, G. (1998). Gamma frequency oscillation in the hippocampus of the rat: intracellular analysis in vivo. Eur. J. Neurosci. *10*, 718–728.

Rash, J.E., Staines, W.A., Yasumura, T., Patel, D., Furman, C.S., Stelmack, G.L., and Nagy, J.I. (2000). Immunogold evidence that neuronal gap junctions in adult rat brain and spinal cord contain connexin-36 but not connexin-32 or connexin-43. Proc. Natl. Acad. Sci. USA *97*, 7573–7578.

Rouach, N., Segal, M., Koulakoff, A., Giaume, C., and Avignone, E. (2003). Carbenoxolone blockade of neuronal network activity in culture is not mediated by an action on gap junctions. J. Physiol. *553*, 729–745.

Shimono, K., Brucher, F., Granger, R., Lynch, G., and Taketani, M. (2000). Origins and distribution of cholinergically induced beta rhythms in hippocampal slices. J. Neurosci. *20*, 8462–8473.

Sik, A., Tamamaki, N., and Freund, T.F. (1993). Complete axon arborization of a single CA3 pyramidal cell in the rat hippocampus, and its relationship with postsynaptic parvalbumin-containing interneurons. Eur. J. Neurosci. *5*, 1719–1728.

Singer, W. (1993). Synchronization of cortical activity and its putative role in information processing and learning. Annu. Rev. Physiol. *55*, 349–374.

Tarnawa, I., Berzsenyi, P., Andrási, F., Botka, P., Hámori, T., Ling, I., and Körösi, J. (1993). Structure-activity relationships of 2,3-benzodiazepine compounds with glutamate antagonist action. Bioorg. Med. Chem. *3*, 99–104.

Tominaga, T., Tominaga, Y., Yamada, H., Matsumoto, G., and Ichikawa, M. (2000). Quantification of optical signals with electrophysiological signals in neural activities of Di-4-ANEPPS stained rat hippocampal slices. J. Neurosci. Methods *102*, 11–23.

Tominaga, T., Tominaga, Y., and Ichikawa, M. (2002). Optical imaging of long-lasting depolarization on burst stimulation in area CA1 of rat hippocampal slices. J. Neurophysiol. *88*, 1523–1532.

Torrence, C., and Compo, G. (1998). A practical guide to wavelet analysis. Bull. Am. Meteorol. Soc. *79*, 61–78.

Traub, R.D., Bibbig, A., Fisahn, A., LeBeau, F.E., Whittington, M.A., and Buhl, E.H. (2000). A model of gamma-frequency network oscillations induced in the rat CA3 region by carbachol in vitro. Eur. J. Neurosci. *12*, 4093–4106.

Traub, R.D., Kopell, N., Bibbig, A., Buhl, E.H., LeBeau, F.E., and Whittington, M.A. (2001). Gap junctions between interneuron dendrites can enhance synchrony of gamma oscillations in distributed networks. J. Neurosci. *21*, 9478–9486.

Traub, R.D., Cunningham, M.O., Gloveli, T., LeBeau, F.E., Bibbig, A., Buhl, E.H., and Whittington, M.A. (2003a). GABA-enhanced collective behavior in neuronal axons underlies persistent gamma-frequency oscillations. Proc. Natl. Acad. Sci. USA *100*, 11047–11052.

Traub, R.D., Pais, I., Bibbig, A., LeBeau, F.E., Buhl, E.H., Hormuzdi, S.G., Monyer, H., and Whittington, M.A. (2003b). Contrasting roles of axonal (pyramidal cell) and dendritic (interneuron) electrical coupling in the generation of neuronal network oscillations. Proc. Natl. Acad. Sci. USA *100*, 1370–1374.

Vessey, J.P., Lalonde, M.R., Mizan, H.A., Welch, N.C., Kelly, M.E., and Barnes, S. (2004). Carbenoxolone inhibition of voltage-gated Ca channels and synaptic transmission in the retina. J. Neurophysiol. *92*, 1252–1256.

Whittington, M.A., and Traub, R.D. (2003). Interneuron diversity series: inhibitory interneurons and network oscillations in vitro. Trends Neurosci. *26*, 676–682.

Whittington, M.A., Traub, R.D., and Jefferys, J.G. (1995). Synchronized oscillations in interneuron networks driven by metabotropic glutamate receptor activation. Nature *373*, 612–615.

Zar, J.H. (1999). Biostatistical analysis, 4th ed (Upper Saddle River, N.J.: Prentice Hall).